NASA Weather Balloon Demonstration of an Additively Manufactured Antenna

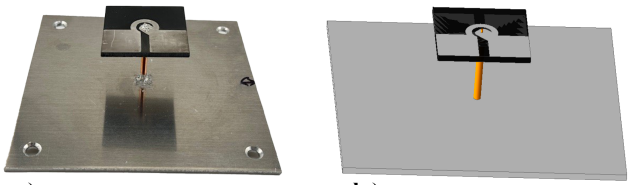
Peter Moschetti [(1)], Alex Moricette[(2)], Tristan T. Epp-Schmidt[(3)], Margaret H. Samuels[(3)], and Verena Gargitter[(4)]

[(1)] Colorado School of Mines, Golden, CO 80401, USA, pmoschetti@mines.edu
[(2)] Florida State University, Tallahassee, FL 32306, USA
[(3)] NASA Goddard, Greenbelt, MD 20771, USA
[(4)] Fortify, Boston, MA 02129, USA

***Abstract*—Additive manufacturing (AM) enables low-cost, lightweight, and geometrically flexible antennas for rapid-deployment missions. This work reports a left-hand circularly polarized magneto-electric dipole printed on a Radix dielectric with inkjet silver metallization and demonstrated as a process replacement for NASA weather-balloon RF hardware. By combining substrate fabrication and metallization, AM provides value for unrecoverable or field-replaceable systems. A physics-based verification workflow links AM-specific material behavior to electromagnetic performance and yields bounded total, radiation, and mismatch efficiencies. Standard surface-impedance and roughness models failed to reproduce the frequency-dependent radiation loss observed in printed inks, underscoring the need for AM-specific conductor parameterization. Mission testing confirmed Tracking and Data Relay Satellite System (TDRSS) link closure from NASA's Columbia Scientific Balloon Facility and validated a repeatable print–measure–fly workflow for bounding RF performance and qualifying AM antennas for field use.**

I. Introduction

Antennas for fielded missions are often constrained by schedule, geometry, and manufacturability. For many missions, hardware is not recoverable. Weather balloons may be lost after landing [1], while military drones [2] and sounding rockets are often destroyed during operation. In these cases, traditional multi-step fabrication imposes cost and schedule penalties that limit design iteration and slow mission tempo. Additive manufacturing offers an alternative [3], providing low-mass, geometry-flexible dielectrics [4], printed metallization [5], [6], and tool-less iteration compatible with rapid print–measure–fly workflows. Current NASA balloon hardware relies on machined dielectric spacers, radomes, and manual tuning, whereas the AM approach reduces fabrication complexity, shortens the development cycle, lowers labor content, and improves part-to-part repeatability. This paper presents an AM magneto-electric (ME) dipole [7]–[9], verifying it in flight, and through a TDRSS link from the Columbia Scientific Balloon Facility. The ME dipole is selected for its planar topology, low-ε_r compatibility, circular polarization, and wide beamwidth [10], [11]. The antenna consists of a Radix dielectric substrate fabricated by vat photopolymerization, with silver conductors inkjet-printed using a BotFactory SV2, and mounted over an aluminum ground plane. The printed substrate is bonded to an SMA four-hole flange RG402 coaxial connector with an 8330S silver epoxy. Measured and modeled results are used to evaluate thin/thick-film and roughness-based conductor models, highlighting a gap in predicting frequency-dependent radiation loss in drop-on-demand printed inks. The antenna was designed in HFSS (Fig. 1(b)), fabricated (Fig. 1(a)), range tested, field tested, and delivered within two months, demonstrating the concept-to-delivery speed achievable with AM.



a.) b.)

Fig. 1: Magneto-electric dipole antenna on a solid Radix substrate ($\varepsilon_r = 2.8$) with printed silver ink: (a) fabricated antenna and (b) HFSS model.

II. Background and Related Work

A. Morphology of Inkjet-Printed Silver Films

Printed silver inks exhibit resistive loss behavior fundamentally different from bulk metals [12]. Areias *et al.* showed that a frequency-dependent, roughness-based $Z_s(f)$ can match aerosol jet printed microstrip lines [13], but their assumptions do not extend to inkjet drop-on-demand films on additively manufactured dielectrics. Materials studies consistently show that inkjet-printed films are porous, granular, and strongly process dependent. The conversion route, drop spacing, temperature, and ink formulation govern grain packing and porosity [14], [15], while layer buildup gradually improves connectivity [16]–[18]. This results in a frequency dependent response that is difficult to predict during the initial design.

This paper attempts to capture these process dependent variables by modeling the conductor as a thin/thick stack [19], [20] with a Groiss roughness correction [21], recovering an effective sheet resistance R_s [22] by decomposing measured efficiencies and calibrating a finite thickness conductor in HFSS [23]. The thin-film and thick-conductor limits are captured in Eq. (1a), with $\delta = \sqrt{2/(\omega\mu_0\sigma)}$ as the skin depth. For a resonant radiator, $R_{\text{in}} \approx R_{\text{rad}} + R_{\text{loss}}$, so $|\Gamma|$ depends only on the total input resistance, not on R_{loss} alone, as shown in Eq. (1c). Increasing R_{loss} slightly shifts R_{in} toward or away

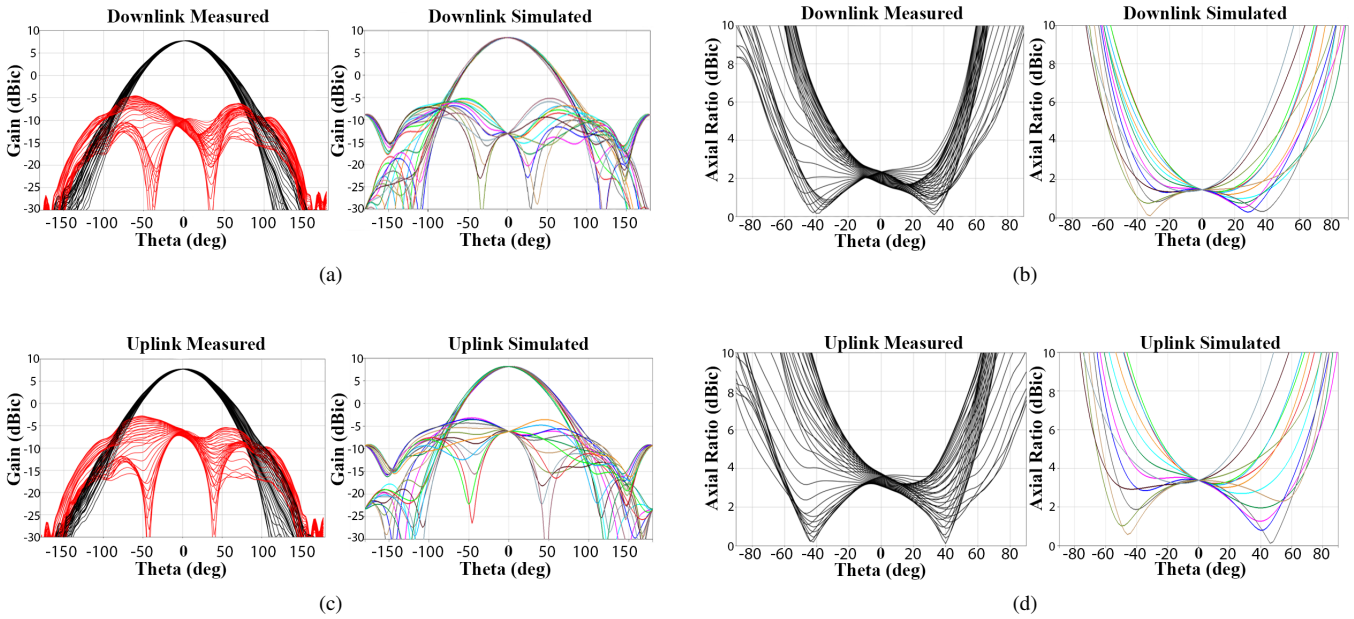


Fig. 2: Measured and simulated far-field results for co-polarized LHCP and cross-polarized RHCP responses at the TDRSS downlink and uplink frequencies for multiple ϕ cuts: (a) downlink realized gain, (b) downlink axial ratio at 2.2875 GHz, (c) uplink realized gain, and (d) uplink axial ratio at 2.1064 GHz.

from 50 Ω but always reduces η_{rad}, as shown in Eq. (1d). Thus, printed silver ink primarily penalizes radiation efficiency, with only weak, non-monotonic signatures in $|\Gamma|$. Because directivity $D(f)$ is pattern-set and only weakly affected by moderate conductor loss, the loss appears experimentally as a frequency-dependent separation between peak gain and peak directivity (Fig. 4), while the input match remains largely unchanged (Fig. 3).

$$R_s(f) = \begin{cases} \sqrt{\pi f\, \mu_0/\sigma}, & t \gg \delta, \\ 1/(\sigma t), & t \ll \delta, \end{cases} \tag{1a}$$

$$R_{\text{loss}} = R_{\text{cond}} + R_{\text{diel}}, \qquad R_{\text{cond}} = R_s \frac{\displaystyle\int_{\mathcal{S}} \|\mathbf{J}_s\|^2 \, \mathrm{d}A}{I_{\text{port}}^2} \tag{1b}$$

$$Z_{\text{in}} \approx R_{\text{in}} = R_{\text{rad}} + R_{\text{loss}} \quad (X \approx 0), \qquad |\Gamma| = \left| \frac{R_{\text{in}} - 50}{R_{\text{in}} + 50} \right| \tag{1c}$$

$$\eta_{\text{rad}} = \frac{R_{\text{rad}}}{R_{\text{rad}} + R_{\text{loss}}}, \quad \eta_{\text{mis}} = 1 - |\Gamma|^2, \quad \eta_{\text{tot}} = \eta_{\text{mis}}\, \eta_{\text{rad}} \tag{1d}$$

III. Antenna Efficiency and Ink Analysis

A. Three-Step Conductor Loss Assessment

This paper used a three-step modeled-to-measured procedure to verify and quantify the impact of printed-ink conductivity, thickness, and roughness on antenna efficiencies and S-parameters.

1) Directivity from measured pattern. Integrate the compact range pattern over (θ, ϕ) to obtain $D(f)$. Verify across 1.9-2.5 GHz that $\eta_{\text{tot}}(f) = \eta_{\text{rad}}(f)\, \eta_{\text{mis}}(f)$ with $\eta_{\text{mis}} = 1 - |\Gamma|^2$.
2) Calibrate Z_s with a layered impedance boundary (HFSS). Choose (σ, t, R_q) to match the measured η_{rad} across the band, thereby establishing the target $R_s(f)$.
3) Transfer to a finite thickness model and recover $|S_{11}|$ shape. Use the same (σ, t) with "Solve Inside" enabled in HFSS, and apply the Groiss roughness model to both outer faces to preserve the calibrated conductor loss while restoring the measured $|S_{11}(f)|$ curvature.

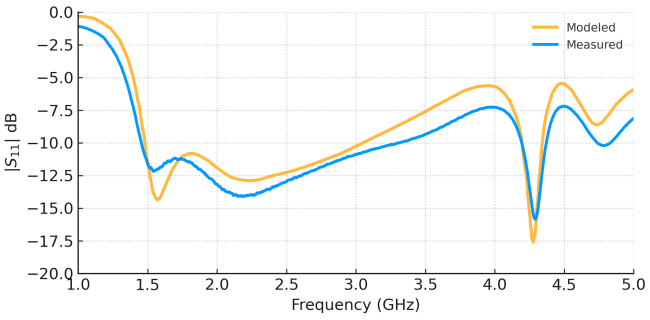


Fig. 3: Measured and modeled $|S_{11}|$ for the solid-Radix substrate antenna.

IV. RF Measurements

Far field antenna patterns and S_{11} were measured in the Goddard Electro Magnetic Anechoic Chamber (GEMAC) at

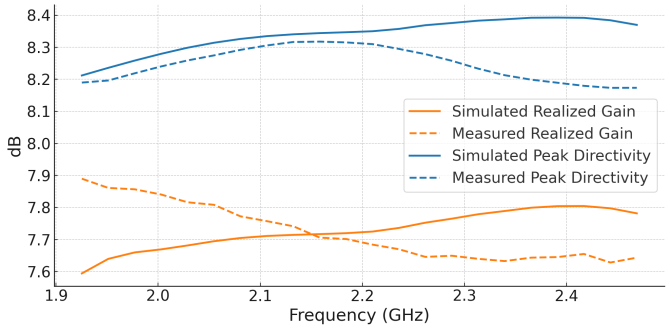


Fig. 4: Measured and simulated peak gain and directivity versus frequency.

NASA Goddard Space Flight Center (GSFC). The measured input match for the antenna is better than -12.5 dB across 2.0 GHz to 2.3 GHz and follows the HFSS response closely (Fig. 3). Displayed gain patterns at the TDRSS bands (2.1064 GHz uplink and 2.2875 GHz downlink) show that the modeled and measured results agree in main beam shape, cross polarization levels, and AR/gain beamwidth (see Figs. 2a–2d). The measured gain and directivity across frequency are shown in Fig. 4. The observed diverging trend in measured vs simulated peak gain, together with the close agreement between measured and simulated directivity, indicates that the dominant frequency-dependent degradation is due to radiation efficiency loss rather than mismatch. Measured total efficiency was obtained by numerically integrating the realized gain and normalizing by 4π. Mismatch efficiency $\eta_{\text{mis}}(f) = 1 - |S_{11}(f)|^2$ was computed from the measured S_{11}, and radiation efficiency was obtained as $\eta_{\text{rad}}(f) = \eta_{\text{tot}}(f)/\eta_{\text{mis}}(f)$, using the measured total efficiency and the mismatch term from S_{11}. By anchoring the simulation with the measured η_{rad} at mid-band and using the three-step process yields an effective sheet resistance for the silver ink of $R_s(f_{\text{mid}}) \approx 5.9\ \Omega/sq$, $t_{\text{top}} = 1\ \mu$m, $\sigma_{\text{top}} = 1 \times 10^4$ S/m, $t_{\text{bulk}} = 8\ \mu$m, $\sigma_{\text{bulk}} = 2 \times 10^4$ S/m, and $R_q = 8\ \mu$m. Figure 5 compares the modeled and measured efficiencies across frequency, showing similar frequency-dependent trends, with the remaining discrepancies attributed to process effects not captured in the simulated model.

A. Error treatment and interpretation

Because classical conductor models could not reproduce the measured frequency-dependent loss, the comparison between HFSS and measurement is re-framed as a quantitative discrepancy analysis rather than model validation. Measured and simulated traces were paired, and band-limited RMSE, MAE, and bias were computed on linear efficiencies over 1.9-2.5 GHz. These metrics (Table I) quantify how far standard electromagnetic models deviate from the true performance of the inkjet-printed antenna. The mismatch term agrees almost exactly, while radiation and total efficiencies do not.

Representative 1σ bounds consistent with compact-range metrology [24] and VNA calibration practice [25] were applied: ± 0.5 dBic for realized gain, ± 0.3 dB for directivity, and ± 0.2 dB for return loss. These uncertainties are far smaller than the observed simulation–measurement discrepancy, indicating that the dominant error is model-driven rather than metrology-driven. Thus, the disagreement is not attributable to measurement noise, frequency interpolation, or pattern-integration uncertainty, but instead reflects missing physics in existing surface-impedance and roughness models when applied to printed conductive inks. Applying Eqs. (2)–(4) to the measured gains, directivities, and reflection coefficients yields the propagated uncertainties used in the comparison metrics of Table I.

TABLE I: Simulation-measurement discrepancy over 1.9–2.5 GHz in linear units.

Metric	RMSE	MAE	Bias	% within ± 0.03
Total	0.0236	0.0212	$+0.0105$	69%
Radiation	0.0285	0.0261	$+0.0197$	59%
Mismatch	0.0070	0.0067	-0.0067	97%

$$\frac{\sigma^2(\eta_{\text{tot}})}{\eta_{\text{tot}}^2} = \left(\frac{\sigma(G_{\text{real}})}{G_{\text{real}}}\right)^2 + \left(\frac{\sigma(D)}{D}\right)^2 \tag{2}$$

$$\sigma(\eta_{\text{mis}}) = 2|S_{11}|\,\sigma(|S_{11}|) \tag{3}$$

$$\frac{\sigma^2(\eta_{\text{rad}})}{\eta_{\text{rad}}^2} = \frac{\sigma^2(\eta_{\text{tot}})}{\eta_{\text{tot}}^2} + \frac{\sigma^2(\eta_{\text{mis}})}{\eta_{\text{mis}}^2} \tag{4}$$

V. Flight Demonstration and Survivability

The antenna was integrated on the weather balloon communications deck and exercised against TDRSS (satellite F6) prior to flight. Mid-latitude link budgets predicted a signal strength window of 9–13 dB. Ground tests returned 13.15–13.33 dB, near the top of the expected range, consistent with chamber-derived efficiencies and LHCP sense. With a transceiver power of 5 W and a data rate of 6 kbps, this corresponds to a measured link margin of $+0.15$ to $+0.33$ dB above nominal. Orientation sweeps with the ME dipole produced transmit strengths of 9.1–10.9 dB (vertical), 15.5–16.0 dB (45° from vertical, 100° azimuth), 14.5 dB (90°/160°), and 11.2 dB (90°/260°), matching the broad main lobe and polarization behavior. On receive, the automatic gain control (AGC) requirement was < 2.0; measurements were 0.9–1.1 at the modem and 0.7–1.1 at the transceiver (worst case 1.5–1.8 at 90° off axis), confirming link margin. The balloon flight carried the same configuration through ascent to the stratosphere and concluded with a successful recovery of the antenna, which incurred minor landing damage.

VI. Conclusion

This work demonstrated a mission-ready, additively manufactured magneto–electric dipole printed on a Radix substrate with inkjet silver metallization and validated through compact-range measurements and a NASA balloon flight. Standard surface-impedance, roughness, and thin/thick-film conductor models reproduce the measured input match but fail to capture the frequency-dependent radiation-efficiency/gain roll-off. The measured gain decreases with frequency despite stable

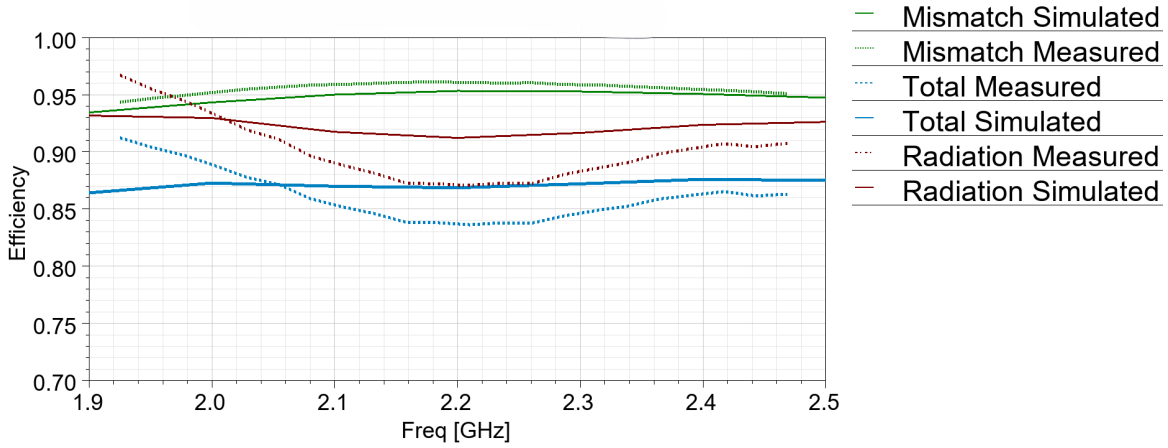


Fig. 5: Measured and simulated mismatch, radiation, and total efficiencies. Mismatch agrees closely, while measured radiation efficiency shows the frequency-dependent loss attributed to the printed silver conductor.

directivity and nearly constant $|S_{11}(f)|$, indicating that the dominant degradation arises from radiation efficiency loss mechanisms in the printed metallization rather than mismatch or pattern distortion. These losses stem from morphology-driven pathways not represented in existing electromagnetic models, highlighting a gap in modeling printed conductive inks and the need for process-specific formulations compatible with full wave solvers. Completing the design, fabrication, range testing, and field validation in only two months demonstrates the accelerated development timelines enabled by AM, while the successful link closure and flight performance, even with post-landing damage, show that AM remains a viable and repeatable approach for rapid RF hardware development.

REFERENCES

[1] D. Schneider, "Chasing downed weather balloons: Hunt them with a cheap SDR receiver and a homemade antenna," *IEEE Spectrum*, vol. 59, no. 9, pp. 16–18, 2022.

[2] M. Z. Chaari, "A growing integration of weaponized commercial drones in battlefield operations," in *Proc. IEEE Int. Workshop Technologies for Defense and Security (TechDefense)*, 2024, pp. 289–294.

[3] J. Persad and S. Rocke, "A survey of 3D printing technologies as applied to printed electronics," *IEEE Access*, vol. 10, pp. 34 603–34 635, 2022.

[4] A. D. Santiago-Vargas, I. H. Abdelaziem, K. Chen, and D. Peroulis, "A broadband high-gain 3D-printed ellipsoidal dielectric lens antenna," in *Proc. IEEE Radio and Wireless Symp. (RWS)*, 2025, pp. 25–28.

[5] J. Siden, M. K. Fein, A. Koptyug, and H. E. Nilsson, "Printed antennas with variable conductive-ink layer thickness," *IET Microwaves, Antennas & Propagation*, vol. 1, no. 2, pp. 401–407, 2007.

[6] C. Blanco-Angulo, A. Martinez-Lozano, J. Arias-Rodriguez, A. Rodriguez-Martinez, J. M. Vicente-Samper, J. M. Sabater-Navarro, and E. Avila-Navarro, "Low-cost direct-writing of silver-based ink for planar microwave circuits up to 10 GHz," *IEEE Access*, vol. 10, 2022.

[7] M. H. Samuels, "3D printed antenna for a balloon test flight," Online, Greenbelt, MD, Oct. 2024, NASA Technical Reports Server (NTRS), Doc. ID 20240012019. [Online]. Available: https://ntrs.nasa.gov/citations/20240012019.

[8] M. Samuels, "3D printed antenna for a balloon test flight," Online, Greenbelt, MD, 2025, NASA Technical Reports Server (NTRS), Doc. ID 20250003783. [Online]. Available: https://ntrs.nasa.gov/citations/20250003783.

[9] K. Murphy, "NASA 3D-printed antenna takes additive manufacturing to new heights," Online, Jan. 2025, [Online]. Available: https://www.nasa.gov/technology/manufacturing-materials-3-d-printing/nasa-3d-printed-antenna-takes-additive-manufacturing-to-new-heights/.

[10] L. Cai, H. Wong, and K.-F. Tong, "A simple low-profile coaxially fed magneto-electric dipole antenna without slot cavity," *IEEE Open Journal of Antennas and Propagation*, vol. 1, pp. 47–58, 2020.

[11] L. Cai and K.-F. Tong, "A single-fed wideband circularly polarized cross-fed cavity-less magneto-electric dipole antenna," *Sensors*, vol. 23, no. 3, p. 1067, 2023.

[12] Y. Shlepnev and C. Nwachukwu, "Roughness characterization for interconnect analysis," in *Proc. IEEE Int. Symp. Electromagnetic Compatibility*, 2011, pp. 518–523.

[13] C. Areias and A. Akyurtlu, "An examination of aerosol jet-printed surface roughness and its impact on the performance of high-frequency electronics," *Advanced Engineering Materials*, 2025.

[14] P. J. Smith, "Inkjet printing silver-containing inks," in *Print4Fab: Printing Future Fab*, 2008, pp. 1–6.

[15] E. Fribourg-Blanc, M. Pélissier, C. Tixier, F. Valdivieso, and F. Volpi, "Characterization of silver nanoparticles based inkjet printed lines," *Microelectronic Engineering*, vol. 110, pp. 247–251, 2013.

[16] R. Kumar, Y. Shin, and L. Yin, "Inkjet-printed Au and Ag electrodes on flexible substrates for electrochemical sensing applications," *Sensors*, vol. 20, no. 5, p. 1333, 2020.

[17] D.-E. Kim, H. Kim, K. Lee, and J. Lee, "Silver nanoparticle conductive inks: Synthesis, characterization, and fabrication of inkjet-printed flexible electrodes," *Scientific Reports*, vol. 10, no. 1, p. 12327, 2020.

[18] K.-S. Sim, J.-H. Choi, S.-H. Yang, H.-J. Lee, and J.-H. Cho, "RF performance of ink-jet printed microstrip lines on rigid and flexible substrates," *Microelectronic Engineering*, vol. 177, pp. 1–7, 2017.

[19] J. R. Corkhill and E. R. O'Donnell, "Effect of process variables on the microwave conductivity of thick-film conductors," *Electronics Letters*, vol. 8, no. 2, pp. 40–42, 1972.

[20] R. B. Keller, *Skin effect*. Cham: Springer, 2023, pp. 135–143.

[21] S. Groiss, I. Bardi, O. Biró, K. Preis, and K. R. Richter, "Parameters of lossy cavity resonators calculated by the finite element method," *IEEE Transactions on Magnetics*, vol. 32, no. 3, pp. 894–897, 1996.

[22] "Sheet resistance—microwave encyclopedia," Microwaves101, [Online]. Available: https://www.microwaves101.com/encyclopedias/sheet-resistance.

[23] ANSYS, Inc., "HFSS, version 2025 R2," ANSYS Electromagnetics Suite, Canonsburg, PA, USA, 2025, [Online]. Available: https://www.ansys.com/products/electronics/ansys-hfss.

[24] C. Parini, M. Salter, D. Janse van Rensburg, and G. Hindman, "Antenna measurement uncertainty method for measurements in compact antenna test ranges," in *Proc. 38th Annu. Meeting Symp. Antenna Measurement Techniques Association (AMTA)*, 2016, pp. 1–6.

[25] EURAMET, "Guidelines on the evaluation of vector network analysers (VNA) (calibration guide no. 12)," EURAMET Calibration Guide, 2018, version 3.0. [Online]. Available: https://www.euramet.org/publications-media-centre/calibration-guidelines.